Cutting off ciliary protein import: intraflagellar transport after dendritic femtosecond-laser ablation

Jona Mijalkovic, Jules Girard, Jaap van Krugten, Jasmijn van Loo, Zhiqing Zhang, Elizaveta Loseva, Felix Oswald, and Erwin J. G. Peterman*
LaserLaB and Department of Physics and Astronomy, Vrije Universiteit Amsterdam, 1081 HV Amsterdam, The Netherlands

ABSTRACT Primary cilia, organelles protruding from the surface of eukaryotic cells, act as cellular antennae to detect and transmit signals from the extracellular environment. They are built and maintained by continuous cycles of intraflagellar transport (IFT), where ciliary proteins are transported between the ciliary base and tip. These proteins originate from the cell body because cilia lack protein synthesis machinery. How input from the cell body affects IFT and ciliary function is not well understood. Here, we use femtosecond-laser ablation to perturb the dendritic input of proteins to chemosensory cilia in living *Caenorhabditis elegans*. Using fluorescence microscopy, we visualize and quantify the real-time response of ciliary proteins to dendritic ablation. We find that the response occurs in three distinct stages. First, IFT dynein is activated within seconds, redistributing IFT components toward the ciliary base; second, the ciliary axoneme shortens and motors slow down; and third, motors leave the cilium. Depletion of ATP by adding azide also results in IFT slowdown and IFT components leaving the cilium, but not in activation of retrograde IFT. These results indicate that laser ablation triggers a specific mechanism important for IFT regulation that allows the cilium to rapidly adapt to changes in the outside environment.

INTRODUCTION

Primary cilia are conserved, membrane-enveloped, microtubule-based organelles projecting from the surface of most eukaryotic cells, with important roles in signaling and sensory perception (Pazour and Witman, 2003; Singla and Reiter, 2006; Bae and Barr, 2008). In cilia, no proteins are synthesized and, consequently, cilia have to receive their building blocks (axonemal precursors, tubulin) and other proteins from the cell body (Wood and Rosenbaum, 2014). Once these ciliary proteins have entered the cilium, they undergo continuous recycling between ciliary base and tip driven by motor proteins in a bidirectional transport process called intraflagellar transport (IFT; Marshall and Rosenbaum, 2001; Scholey, 2003; Qin *et al.*, 2004; Hao *et al.*, 2011; Buisson *et al.*, 2013). IFT is necessary for ciliary maintenance and assembly. Although IFT has been thoroughly investigated, few studies have addressed how input from the cell body affects IFT and ciliary function.

In *Caenorhabditis elegans*, chemosensory cilia emanate from the dendritic endings of sensory neurons. These cilia contain axonemes with a so-called 9+0 structure: 9 microtubule doublets form the proximal or middle segment and 9 microtubule singlets extend to form the distal segment without a central pair. Two motors of the kinesin-2 family, kinesin-II and OSM-3, cooperate to drive anterograde IFT from the ciliary base to the distal tip (plus end of microtubules; Snow *et al.*, 2004; Pan *et al.*, 2006; Prevo *et al.*, 2015), whereas one retrograde motor, IFT dynein, returns cargo from the tip to the base (minus end; Signor *et al.*, 1999). Motors and IFT particles A and B form complexes, called IFT trains, that transport cargo along the

ciliary axoneme. Although the *C. elegans* ciliary membrane appears to extend into the plasma membrane, there is growing evidence that the cilium is separated from the dendrite and cell body (site of protein synthesis) by a selective periciliary diffusion barrier (Nachury et al., 2010). This raises questions about the role of the cilium as a compartment within the larger neuronal transport system extending from the cell body to the ciliary tip: how is ciliary trafficking regulated and how is it affected by dendritic input?

To address these questions, we perturbed the connection between cell body and cilium by femtosecond-laser ablation of *C. elegans* chemosensory dendrites. Femtosecond-laser ablation has previously been demonstrated to be a high-precision tool to mechanically perturb biological systems with minimal collateral damage (Vogel et al., 2005; Bourgeois and Ben-Yakar, 2008; Gattass and Mazur, 2008). In *C. elegans*, pulsed femtosecond lasers have shown to be particularly useful in investigating the role of specific motor neurons, sensory neurons, and neuronal pathways. In these studies, hours or days after the severing of cell bodies (Chung et al., 2013), axons (Yanik et al., 2004), or dendrites (Chung et al., 2006), worm behavior was observed and evaluated. Ciliary signaling and IFT, however, occur on much more rapid time scales (seconds). Here, we use femtosecond-laser ablation of dendrites of ciliated neurons, in combination with fluorescently labeled ciliary proteins to probe the real-time ciliary response to dendritic input. We observe a rapid response to dendritic ablation that occurs in three distinct stages: a primary stage (seconds), during which IFT motors redistribute with normal velocity; a secondary stage (tens of seconds), during which the axoneme shortens and motor velocities are reduced while the motors remain in the cilium; and a tertiary stage (several minutes) characterized by motor efflux from the cilium. The secondary and tertiary response are also observed in experiments where ATP is depleted by azide addition, indicating that these longer time-scale responses are, at least in part, ATP-mediated. Laser ablation, however, triggers a specific ATP-independent mechanism activating retrograde IFT, resulting in a rapid redistribution of IFT components. This mechanism might enable the cilium to rapidly adapt to changes in the extracellular environment.

RESULTS AND DISCUSSION
Femtosecond-laser ablation of *C. elegans* phasmid chemosensory dendrites
To investigate the ciliary response to abrupt changes in dendritic input, we performed femtosecond-laser ablation of the dendrites of phasmid chemosensory neurons in the *C. elegans* tail (Figure 1, A and B, and Supplemental Figure 1A). We chose tail neurons because of the lower density of neurons here compared with in the head, which allowed for ablation with minimal effects on surrounding neurons. *C. elegans* has two pairs of phasmid cilia referred to as the left (PHAL and PHBL) and right (PHAR and PHBR) pair with overlapping distal segments (Figure 1A). We initially ablated both dendrites of the phasmid pair because the effects of severing only one are obscured in the distal segment due to the overlap. To visualize IFT in real time pre- and postablation, we used epifluorescence microscopy of *C. elegans* strains (Prevo et al., 2015) endogenously expressing fluorescently tagged tubulin (TBB-4::EGFP; Hao et al., 2011; Mijalkovic, 2018), IFT dynein (XBX-1::EGFP; Mijalkovic et al., 2017), OSM-3 (OSM-3::mCherry; Prevo et al., 2015), and IFT-particle subcomplex B (IFT-B; OSM-6::EGFP; Prevo et al., 2015). From the image sequences obtained, we generated time-averaged fluorescence images and kymographs using *KymographClear* (Mangeol et al., 2016).

Ciliary motors and IFT particles are actively transported to the base after dendritic ablation
First, we focused on the initial, short-term ciliary response to dendritic perturbation. Animals from the strains investigated were measured continuously at low fluorescence excitation intensity for 60–90 s postablation. Preablation, IFT dynein and IFT-B are found throughout the proximal and distal segments with accumulation at the ciliary base and transition zone (Figure 1C), concurrent with previous reports (Schafer et al., 2003; Prevo et al., 2015). Visual inspection of the time-averaged fluorescence image sequences postablation reveals that IFT dynein and IFT-B are redistributed within 60 s: the fluorescence intensity appears to decrease in the distal segment and increase in the middle segment and ciliary base (Figure 1C). Tubulin shows a similar redistribution, but less strikingly so than IFT dynein and IFT-B.

To quantify the redistribution of the ciliary components, we plotted the average fluorescence intensity along the cilium pre- and postablation for IFT dynein, IFT-B, OSM-3, and tubulin. For IFT dynein and IFT-B, we observe a decrease of the fluorescence intensity in the distal and proximal segments and a concomitant increase at the base and transition zone (Figure 1D) postablation. These results indicate that IFT dynein and IFT-B redistribute within the cilium in response to dendritic ablation, with the total amount of these components remaining relatively constant. For tubulin, we observe a decrease in fluorescence intensity in the distal segment, consistent with axonemal shortening (Figure 1D). The kinesin-2 motor OSM-3 has a markedly different distribution compared with IFT dynein and IFT-B and is located mainly in the distal segment (Figure 1C; Snow et al., 2004; Prevo et al., 2015). Therefore, we wondered whether OSM-3 would behave differently in response to ablation. Like IFT dynein and IFT-B, OSM-3 also appears to move away from the distal segment within 60 s, occupying the base and proximal segment in a similar distribution to IFT dynein and IFT-B and retracting at a similar rate (Figure 1, C and D). The unusual positioning of OSM-3 at the ciliary base postablation suggests that it remains bound to IFT trains containing IFT dynein upon redistribution.

To obtain insight into the dynamics of the motor and particle redistribution, we generated kymographs of IFT-dynein and IFT-B movement in the cilium, pre- and postablation (Figure 1, E and F). The kymographs show a remarkably sudden reflux of both components within seconds after ablation, as can be seen by the increase in retrograde IFT frequency (more retrograde trains per second). Initially, this reflux has a similar velocity to preablation, IFT-dynein–driven retrograde transport (kymograph lines are parallel pre- and postablation). After ~15 s postablation, kymograph lines become increasingly less steep, indicating a slowing down of IFT. These results suggest that ablation of dendrites of ciliated chemosensory neurons triggers the active return of IFT dynein within the cilium toward the base, while taking along other IFT components.

Motor and IFT-particle redistribution is not triggered by axonemal collapse
To probe whether the redistribution of motors and particles could be caused by the collapse of the ciliary axoneme, we compared axoneme length with the locations of motors and particles, obtained from the time-averaged fluorescence image sequences (Figure 1G). Preablation, the motors (IFT dynein: 7.73 μm ± 0.20 μm; OSM-3: 8.03 μm ± 0.42 μm, average ± SEM) and IFT-B (8.05 μm ± 0.15 μm), cover the complete length of the ciliary axoneme (7.43 μm ± 0.16 μm). Postablation, however, IFT-dynein and IFT-B redistribute rapidly, at almost identical rates. After 15 s, the IFT components extend to only 75–80% of the preablation cilium length (Figure 1G). In comparison, the ciliary axoneme reduces only slightly, to 91% of its preablation
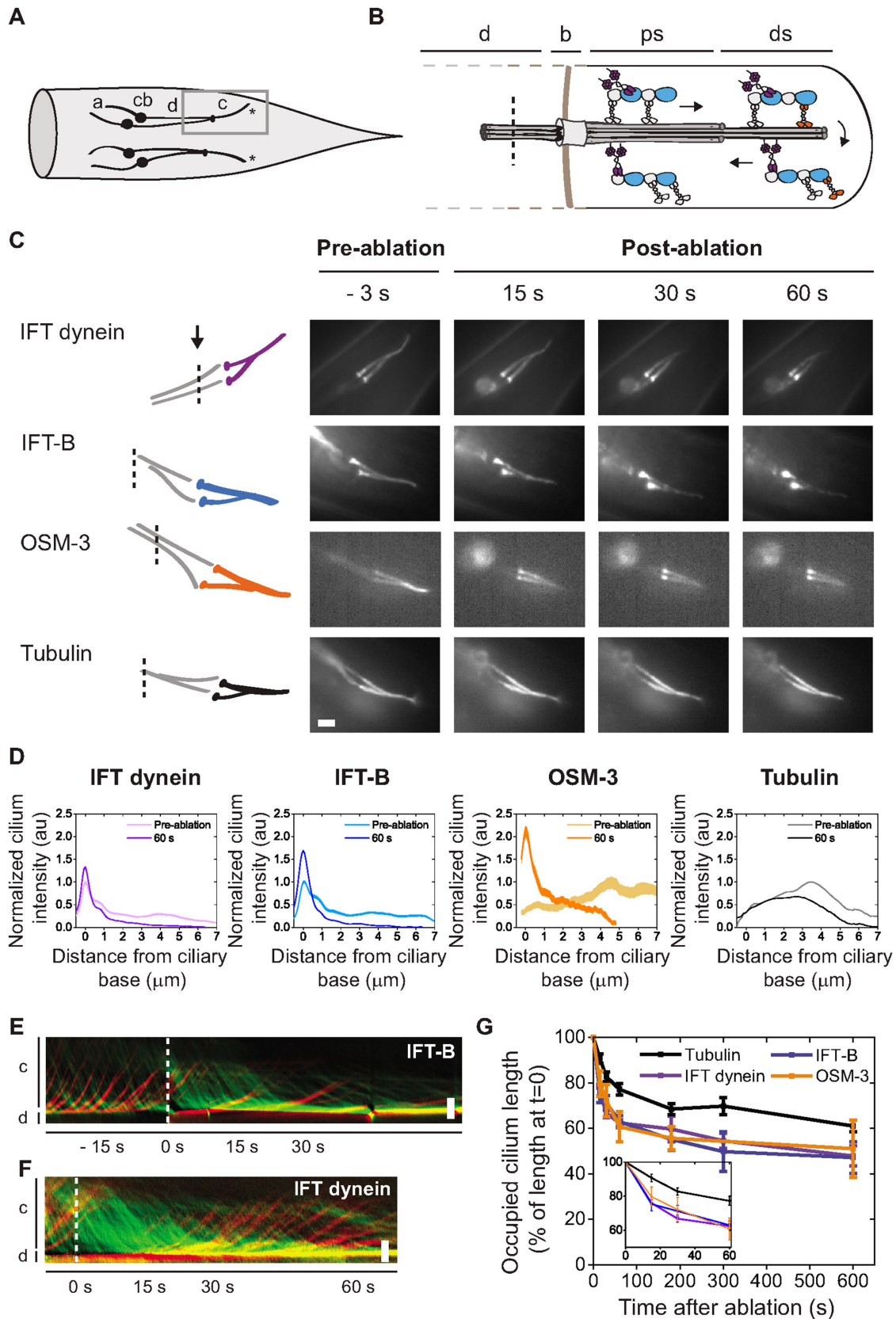
FIGURE 1: Primary response of IFT dynein, IFT-B, and tubulin to femtosecond-laser ablation of *C. elegans* chemosensory dendrites. (A) Cartoon schematic of *C. elegans* tail phasmid neurons: a, axon; cb, cell body; d, sensory dendrite; c, cilium; *, ciliary tip. (B) Zoom-in schematic of the cilium, the region indicated by the gray box in A, focusing on IFT. d, sensory dendrite; b, base; ps, proximal segment; ds, distal segment; tan: pericilliary diffusion barrier; dotted tan line: pericilliary membrane; dotted gray line, cell membrane; dotted black line, approximate position

length. After 60 s, IFT dynein, OSM-3, and IFT-B retract to approximately 62%, while the axoneme has shortened to 77% (Figure 1, F and G). These results show that shortening of the ciliary axoneme is significantly slower than motor and IFT-B retraction, suggesting that the redistribution of IFT proteins is not triggered by the axonemal collapse. Instead, our data suggest that dendritic ablation triggers a cellular signal that stimulates the almost immediate redistribution of IFT motors and IFT particles within the cilia. The absence of motors and particles in the ciliary tip subsequently results in a depletion of components essential for axonemal maintenance, causing the axonemal microtubules to collapse and shorten.

After the initial shortening of the axoneme in the first minute postablation, the cilium continues to shorten but at a significantly slower rate (Figure 1G). After 10 min, the axoneme is shortened to ~60% of its preablation length and does not further shorten (at least until after 60 min). This means that the distal segment has gradually disappeared and only the proximal segment is left. To further assess the role of the proximal segment in response to perturbation, we ablated dendrites in an *osm-3* (mutant) strain, which lacks the distal segment (Supplemental Figure 1, A and B; Perkins *et al.*, 1986; Snow *et al.*, 2004). We determined the ciliary distance occupied by IFT-dynein motors in this strain postablation and found that it does not significantly differ from the distance occupied preablation (Supplemental Figure 1C). Together, these findings show that, while the ciliary distal segment responds within tens of seconds to ablation, the proximal segment stays intact. This indicates that the proximal segment forms a stable structure that does not rapidly disassemble in response to perturbations.

Motor redistribution is not affected by Ca²⁺ chelation

It is well established that cilia play important roles in a myriad of signaling processes (Nachury and Mick, 2019). Ion channels (Qin *et al.*, 2005), TGF-β receptors (Dalfo *et al.*, 2012; Clement *et al.*, 2013), receptor tyrosine kinases (RTKs; Schneider *et al.*, 2005), and GPCRs (Ye *et al.*, 2013; Schou *et al.*, 2015) are expressed in various types of primary cilia. Moreover, there is evidence that signal-transduction molecules can modify ciliary length and structure (Mukhopadhyay *et al.*, 2008). It is therefore plausible that the rapid activation and redistribution of IFT-dynein motors that we observe on the subsecond and seconds time scales are induced by a signaling cue. In *Chlamydomonas* it has been shown that an increase in Ca²⁺ in the flagella can trigger retrograde IFT (Collingridge *et al.*, 2013). To probe whether the redistribution of IFT components in our experiments is Ca²⁺-mediated, we depleted Ca²⁺ in the buffer and imaging pads using the chelator ethylene glycol tetraacetic acid (EGTA). Worms treated with 100 mM EGTA were subjected to femtosecond-laser ablation and fluorescence imaging, performed as described

above (Supplemental Figure 2). Average fluorescence intensities of IFT dynein (Supplemental Figure 2, A and B) show a redistribution of IFT dynein from the distal to the proximal segment, similar to that observed in the ablation experiments without Ca²⁺ chelation (Figure 1, C and D). Kymographs of IFT-dynein dynamics pre- and postablation in the presence of EGTA (Supplemental Figure 2C) reveal an increase in retrograde frequency postablation, similar to the experiments in the presence of Ca²⁺ (Figure 1F). Taken together, our data show that the sudden IFT-dynein reflux postablation occurs in both the presence and absence of extracellular Ca²⁺, which might indicate that it is not triggered by changing Ca²⁺ levels.

Ciliary motors slow down but do not exit the cilium after dendritic ablation

Next, we ablated only one dendrite within a phasmid pair as a control for damage to surrounding cells and to validate the precision of the instrument. The dendrites of the phasmid pair usually overlap (Figure 1C), but depending on worm orientation and cellular architecture, the dendrites can be up to 3 μm apart, allowing for the ablation of a single dendrite (Figure 2, Supplemental Figure 1, and Supplemental Movie 1). When only a single dendrite of a pair is ablated in *wild-type* (Figure 2, A–D) or *osm-3* (mutant) nematodes (Supplemental Figure 1, D–H), IFT dynein is substantially redistributed in the cilium emanating from the ablated dendrite, but not in the second cilium. After ablation (24 h), the unablated dendrite and its emanating cilium have remained intact (Supplemental Figure 1H), indicating that there is minimal damage to cells surrounding the ablated neuron. In some worms, the IFT-dynein fluorescence intensity at the ciliary base and transition zone is slightly increased just after ablation (Figure 2, A–D), which might be due to local heating caused by the ablation process. This effect is, however, very small compared with that seen in the cilia of ablated dendrites. We observed the same ciliary shortening and IFT-motor redistribution in cilia where only a single dendrite was ablated as when both were ablated (Figures 1 and 2 and Supplemental Figure 1), further validating our earlier findings. Similarly, we observed IFT-motor redistribution both in the presence and absence of Ca²⁺ when a single dendrite was ablated (Supplemental Figure 2, D–H). We next investigated how dendritic ablation affects IFT velocity. To this end, we generated kymographs from IFT-dynein fluorescence image sequences (Figure 2, A–D) and compared anterograde (red) and retrograde (green) movement in control cilia with that of dendrite-ablated cilia, within the same phasmid cilium pair. Preablation, anterograde (IFT dynein carried as cargo by kinesin motors) and retrograde (dynein actively driving IFT trains) velocities of control and ablated cilia are undistinguishable (Figure 2, A, E, and H). Immediately after ablation, motor velocities are unaltered but the

of laser cut. (C) Left, cartoons showing position of the focus of the ablation laser (dotted line) in the dendrites shown right. Right, representative summed fluorescence intensity images of IFT dynein (XBX-1::EGFP), IFT-B particle subcomplex (OSM-6::EGFP), OSM-3 (OSM-3::mCherry), and tubulin (TBB-4::EGFP) in the dendrite and phasmid cilium, pre- and postablation. Scale bar: 2 μm. (D) Averaged, normalized cilium fluorescence 3 s preablation and 60 s postablation of IFT dynein (purple, *n* = 20 cilia from 19 worms), IFT-B (blue, *n* = 11 cilia from 11 worms), OSM-3 (orange, *n* = 5 cilia from 5 worms), and tubulin (black, *n* = 20 cilia from 20 worms). Line thickness is SEM. (E, F) Representative IFT-B (E) and IFT-dynein (F) kymographs showing retrograde (green) and anterograde (red) motility. Horizontal: time; vertical: position. Scale bar: 2 μm. Moment of ablation is indicated by the dotted line. (G) Tubulin redistribution as percentage of preablation cilium length (preablation: *n* = 20 cilia; postablation: 15 s, *n* = 20; 30 s, *n* = 20; 60 s, *n* = 19; 180 s, *n* = 13; 300 s, *n* = 13; 600 s, *n* = 17), and IFT dynein (preablation: *n* = 20 cilia; postablation: 15 s, *n* = 18; 30 s, *n* = 20; 60 s, *n* = 19; 180 s, *n* = 9; 300 s, *n* = 13; 600 s, *n* = 12), OSM-3 (*n* = 5 cilia), and IFT-B (preablation: *n* = 11 cilia; postablation: 15 s, *n* = 11; 30 s, *n* = 9; 60 s, *n* = 7; 180 s, *n* = 11; 300 s, *n* = 6; 600 s, *n* = 6) redistribution as percentage of preablation occupied ciliary distance. Inset: first 60 s postablation.
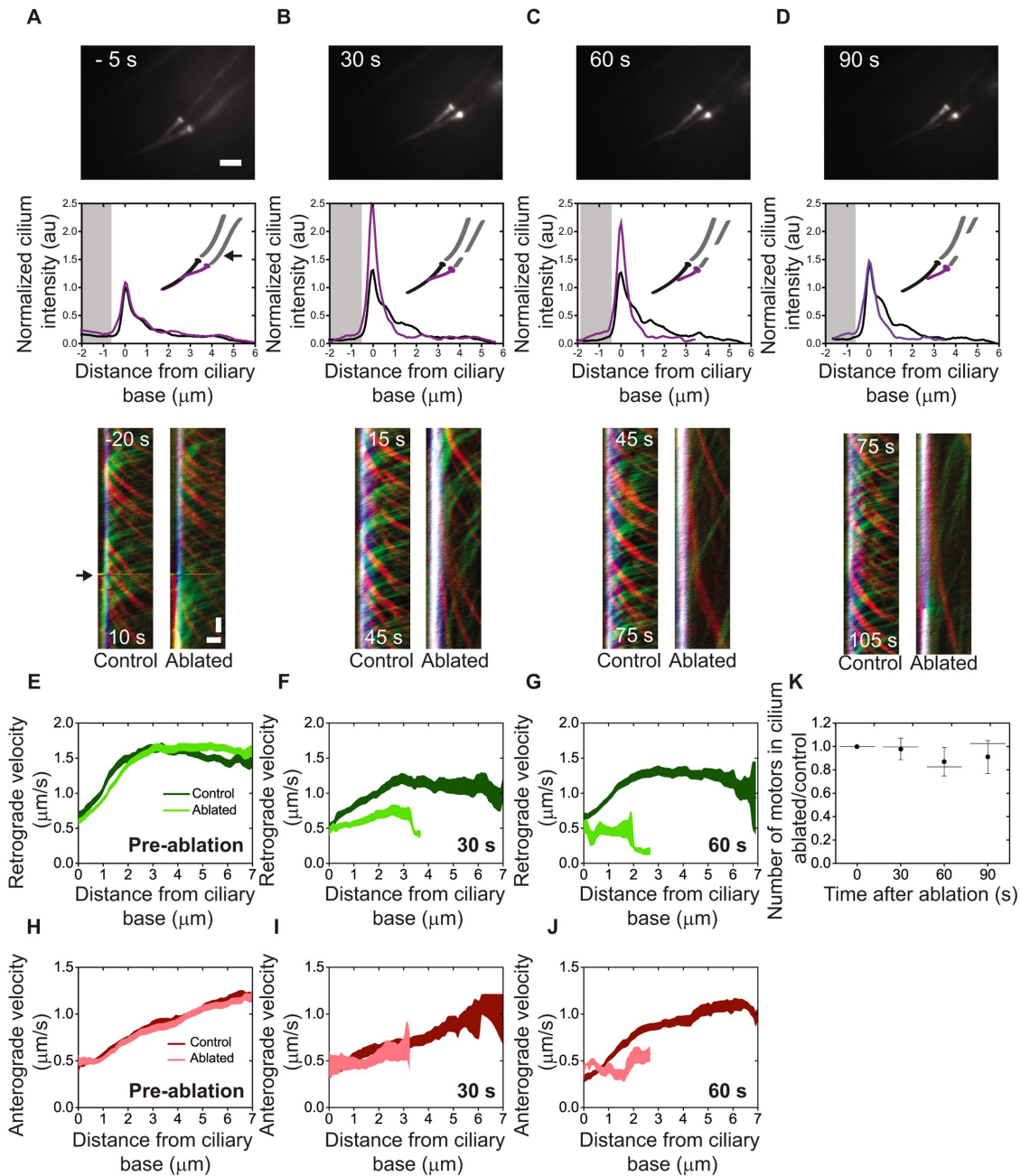
FIGURE 2: IFT-dynein redistribution and slowdown. (A–D) Representative summed IFT dynein (XBX-1::EGFP) fluorescence images (scale bar: 2 µm) and kymographs (Time: vertical; scale bar = 2 s. Position: horizontal; scale bar = 1 µm) 5 s preablation (A), and 30 s (B), 60 s (C), and 90 s (D) postablation of the ablated and nonablated (control) cilium. Gray area indicates the dendrite. (E–G) Retrograde velocity in the control (dark green) and ablated (light green) cilium. (F–J) Anterograde velocity in the control (dark red) and ablated (light red) cilium. Error is SEM. (K) Ratio of ablated/control total number of IFT dyneins in the cilium pre- and postablation. Dot: average; error bar: 95% confidence interval; line, median. See also Supplemental Movie 1.

frequency of retrograde IFT trains increases suddenly, resulting in IFT-dynein redistribution (as observed in cilia with both dendrites ablated; Figure 1H). From approximately 15 s after ablation, both retrograde and anterograde velocities start to decrease compared with control (Figure 2, B, C, F, G, I, and J). After ablation (90 s), IFT is still active but motors are at least twice slower, as can be seen from the increased slope of the kymograph lines (Figure 2D). The slowing down could be triggered by the intracellular signaling response. For example, dauer pheromone and Gα-protein signals have been shown to alter kinesin-II and OSM-3 velocities in *C. elegans* larvae

(Burghoorn *et al.*, 2010). A more likely explanation, however, is that motors slow down due to the loss of ATP in the cilium, which is thought to be supplied from the dendrite. Without an external supply of ATP, we would expect that ATP is almost completely converted into ADP within ~2 s (assuming that only a fraction [~10%] of ciliary motors are active [~240 of the in total ~2400 kinesin-II, OSM-3, and IFT dynein motors in total]; Prevo *et al.*, 2015; Mijalkovic *et al.*, 2017) at a given time, with an ATP-hydrolysis rate of 10–30 s^{-1} (Johnson, 1983; Gilbert *et al.*, 1995; Imanishi *et al.*, 2006), and assuming that the ATP concentration in the cilium is ~2 mM, and the
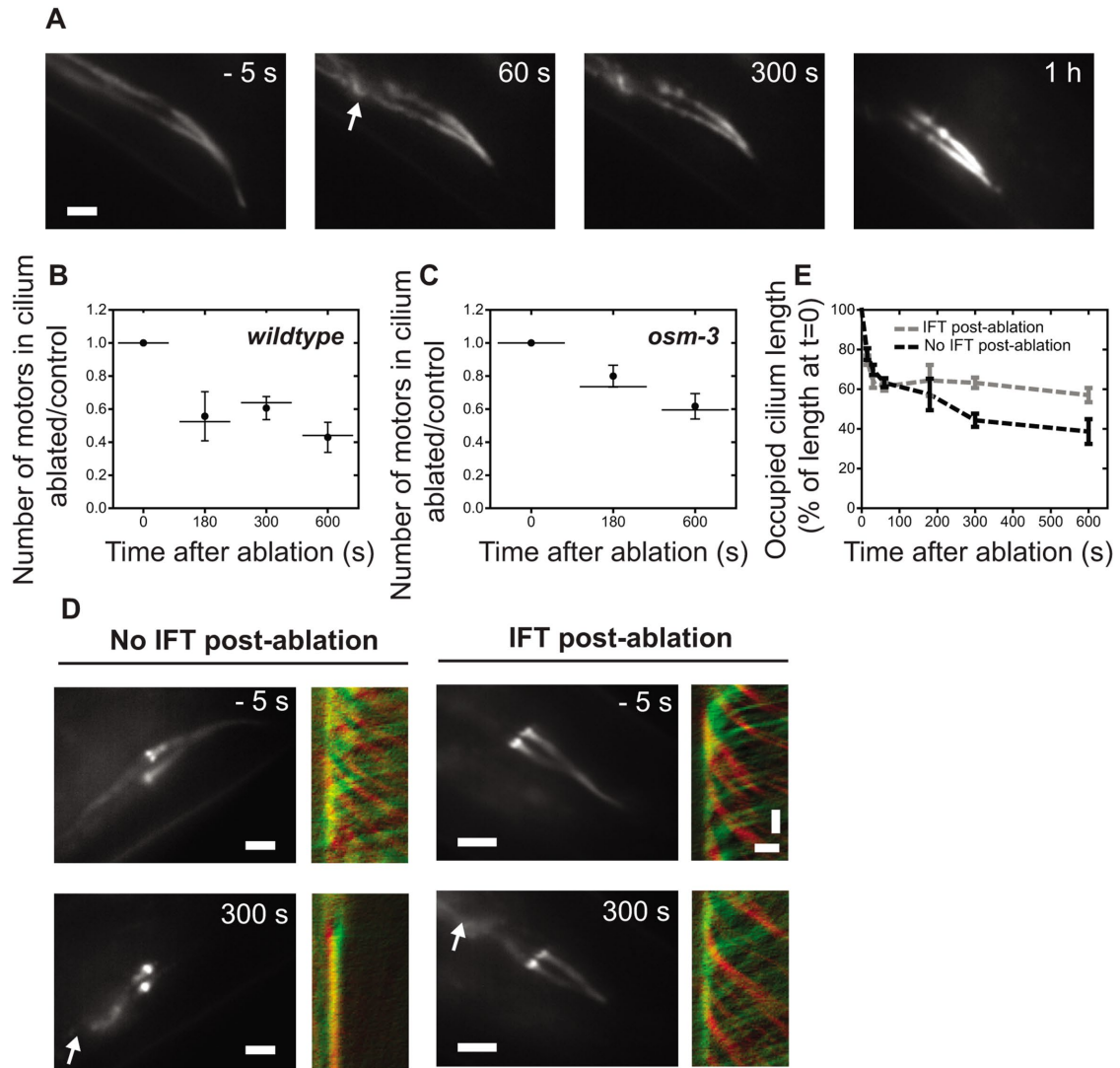
FIGURE 3: Tertiary response to dendritic ablation. (A) Representative summed tubulin (TBB-4::EGFP) fluorescence images pre- and postablation (−5, 60, 300 s, and 1 h). (B, C) Ratio of ablated/control total number of XBX-1 in the cilium pre- and postablation in *wild-type* (B) and *osm-3* (C) worms. Dot: average; error bar: 95% confidence interval; line: median. (D) Representative summed IFT dynein (XBX-1::EGFP) fluorescence images (scale bar = 2 μm) and corresponding kymographs of movement in the proximal segment in cilia with and without active IFT, 300 s postablation (horizontal scale bar = 1 μm; vertical scale bar = 2 s). Green: retrograde transport; red: anterograde transport. Arrow indicates position of laser ablation. (E) IFT-dynein retraction (percentage of preablation distance occupied along cilia), with active IFT (gray dotted line, $n = 10$) and without active IFT (black dotted line, $n = 10$) after 300 s. Error: SEM.

volume of the cilium is ~4×10^{-19} l). This appears to be an order of magnitude faster than we observed (approximately tens of seconds). It is likely that in vivo IFT trains, which are composed of tens of motors, can continue moving longer after ATP depletion than individual motors.

We then used the cilium-averaged integrated fluorescence intensity to calculate the total number of dyneins in unablated and ablated cilia at different time points after ablation, using the unablated cilium as a bleaching control for each time point. We find that in *wild-type* worms the ablated/control motor number ratio is close to 1 up to 90 s after ablation (Figure 2K), implying that most motors remain in the cilium. Similarly, in *osm-3* worms, most motors (~80%) remain in the cilium (Supplemental Figure 1I). These results support our previous observations of motor redistribution (Figure 1D and Supplemental Figure 1B) and show that most motors, at least up to

90 s after ablation, do not exit the cilium but remain available at the ciliary base and proximal segment for IFT.

The tertiary response to dendritic ablation

So far, we have mainly focused on the first tens of seconds following femtosecond-laser ablation of phasmid dendrites and described and quantified the primary (fast redistribution of IFT components toward ciliary base) and secondary (slowing down of IFT) events. In the following, we will describe and quantify the tertiary response, in the tens of minutes afterward. First, we determined whether the proximal segment remains stable on longer time scales (tens of minutes) after ablation. Figure 3A shows that the ciliary axoneme does not shorten further than 55.6% ± 5.8% ($n = 6$) of the preablation length, 1 h postablation. This confirms that the proximal segment of the axoneme, which consists of microtubule doublets, remains

A

Pre-dosing | Post-dosing

-3 s | 15 s | 30 s | 60 s | 180 s

IFT dynein

High

Medium

Low

Control

B

(Occupied) cilium length (% of length at t=0)

IFT dynein

Tubulin

Control
Low
Medium
High

Time after dosing (s)

C

Control — Pre-dosing, 30 s, 60 s
Low — Pre-dosing, 30 s, 60 s
Medium — Pre-dosing, 30 s, 60 s
High — Pre-dosing, 30 s, 60 s

Normalized cilium intensity (au)

Distance from ciliary base (μm)

D Low
E Medium
F High

Number of motors in cilium treated/control

Time after treatment (s)

G Pre-dosing
H 30 s
I 60 s

Retrograde velocity (μm/s)

Control
Low
Medium
High

Distance from ciliary base (μm)

J Pre-dosing
K 30 s
L 60 s

Anterograde velocity (μm/s)

Distance from ciliary base (μm)

stable in response to the perturbation. In addition, 10 min after perturbation only half of the IFT dynein motors have left the cilium in both *wild-type* (Figure 3B) and *osm-3* (Figure 3C) worms. These findings highlight that, even on longer time scales, a considerable amount of IFT motors stays inside the cilium. Retaining the motors and their track could allow the cilium to reactivate IFT if the perturbation is temporary or reversible, or continue disassembly (at a slower rate) in the case of an irreversible perturbation such as our and others' (Chung *et al.*, 2006) dendritic ablations. The *C. elegans* chemosensory cilium appears to be ideally equipped for such a bimodal response: it consists of a proximal segment, composed of microtubule doublets in a stabilized axonemal structure and a distal segment built of dynamic microtubule singlets that can rapidly disassemble (Hao *et al.*, 2011). *Chlamydomonas* cilia lack such a bipartite structure, yet appear to also respond in a stepwise manner to chemical perturbations: after the addition of sodium chloride or sodium pyrophosphate, *Chlamydomonas* cilia first retract to approximately 50% of their length, followed by a slower, long-term retraction (although both happen at longer time scales than in our experiments; Solter and Gibor, 1978). This suggests that the rate of ciliary shortening in response to stimuli is not necessarily determined by axonemal structure, but could also be influenced by other factors, such as the number of motors.

Next, we assessed the long-term effects of dendritic ablation on IFT. In the first minute postablation, the motors move with reduced velocity in all measured cilia (Figure 2, E–J). Remarkably, after 5 min, IFT resumed in some cilia but not in others (Figure 3D). To better understand this heterogeneity, cilia were grouped based on whether IFT reactivates or not after 5 min and the lengths of the regions of the cilia occupied by motors were determined. The initial rate of motor retraction does not seem to differ between the two groups of cilia (Figure 3E), confirming that primary and secondary response are relatively homogeneous in all ablated cilia. After 180 s postablation, however, two distinct scenarios unravel. In cilia where IFT reactivates, the IFT dynein stops retracting and remains occupying ~60% of the cilium length (Figure 3E). In contrast, in cilia where IFT does not resume, the IFT dynein motors continue retracting toward the base (Figure 3E). It is possible that, in the group with reactivated IFT, the dendrite was only partially severed. Another possibility is that, in some cases, glycolytic enzymes can take over the production of ATP when ATP is no longer available from the dendrite, reactivating IFT in some cilia. It is currently not known whether glycolytic enzymes are present in *C. elegans* chemosensory cilia, but their activity has been reported in the outer segments of mammalian photoreceptor cells (Hsu and Molday, 1991) and in *Chlamydomonas* flagella (Mitchell *et al.*, 2005).

To test to what extent the ciliary response to dendritic ablation is caused by a decreased ATP concentration, we chemically depleted ATP, by pipetting sodium azide solutions with different concentrations or M9-buffer (as a control) on worms, while monitoring IFT with fluorescence microscopy as above (Figure 4, Supplemental Figure 3, and Supplemental Movie 2). Time-averaged fluorescence image sequences reveal substantial changes in fluorescence intensity postdosing (Figure 4A). To get more insight into these changes, we determined the length of the cilium occupied by IFT dynein and the length of the axoneme (Figure 4B and Supplemental Figure 3A). These data show shortening similar to the laser-ablation experiments (Figure 1G), on a similar time scale. The shortening was more pronounced at higher concentrations of azide. Average fluorescence intensities of IFT dynein (Figure 4C) and OSM-3 (Supplemental Figure 3, A and B) indeed show that the motors gradually leave the distal segment. In contrast to the large redistribution of the motors toward the ciliary base after laser ablation (Figures 1, D and F, and 3), the motor profiles show an even decrease in intensity all over the cilium, in an azide concentration–dependent way. IFT-dynein retrograde (Figure 4, G–I) and anterograde velocities (Figure 4, J–L) decreased with increasing azide concentration, as expected at decreasing ATP concentration. Taken together, these azide experiments indicate that some but not all effects of dendritic laser ablation can be explained by ATP depletion.

An overall picture that emerges is of a multistep ciliary response to dendritic ablation (Figure 5). In a primary response, within one to two IFT cycles (15 s) dynein motors are triggered to retract from the distal segment to the base and proximal segments at normal velocity, taking with them OSM-3 motors and IFT-B particles. Within seconds, the ciliary axoneme starts to disassemble from the distal tip. In a secondary response, after 7–10 IFT cycles (60–90 s), motors slow down but are retained in the cilium, allowing rapid restoration of IFT in part of the ablated cilia. If the damage to the dendrite is permanent, motors will, in a tertiary response, leave the cilium, while the proximal segment doublet microtubule structure does not shorten further. Azide experiments indicate that the secondary and tertiary responses are likely caused by loss of ATP due to severing of the supply via the dendrite. The primary response, fast activation of retrograde transport, might point at a more specific IFT regulatory mechanism.

We have shown here that dendritic femtosecond-laser ablation, despite being an artificial cue, can lead to the activation of biological signaling pathways that modulate ciliary function. In mammalian cells and *Chlamydomonas*, cellular calcium levels were found to affect cilium length (Johnson and Rosenbaum, 1993; Besschetnova *et al.*, 2010), a finding supported by computational models (Ludington *et al.*, 2015). Moreover, the phosphorylation of FLA8,

FIGURE 4: The effect of ATP depletion on IFT dynein. (A) Left, cartoon showing sodium azide treatment. Right, representative summed fluorescence intensity images of IFT dynein (XBX-1::EGFP) in phasmid cilia, pre- and posttreatment with sodium azide. Scale bar = 2 μm. (B) Top, IFT-dynein redistribution as percentage of pretreatment occupied ciliary distance. Control (black), $n = 9$ cilia; low azide concentration (olive), $n = 7$; medium azide concentration (blue), $n = 14$; high azide concentration (orange), $n = 11$. Bottom, tubulin redistribution as percentage of pretreatment cilium length. Control (black), $n = 8$ cilia; low azide concentration (olive), $n = 7$; medium azide concentration (blue), $n = 13$; high azide concentration (orange), $n = 9$. (C) Averaged, normalized cilium fluorescence of IFT dynein 3 s predosing (light purple), 30 s postdosing (purple), and 60 s postdosing (dark purple) in control (M9-treated) worms (top left) and azide-treated worms (top right, bottom left, bottom right). Line thickness is SEM. (D–F) Ratio of treated/control total number of IFT dyneins in the cilium pre- and postdosing at low (olive, D), medium (blue, E), and high (orange, F) azide concentration. Dot: average; error bar: SEM. (G–I) Retrograde velocity pretreatment (G) and posttreatment (H, I) with azide. (J–L) Retrograde velocity pretreatment (J) and posttreatment (K, L) with azide. Line thickness is SEM. For C–L, control, $n = 9$ cilia; low azide concentration, $n = 7$; medium azide concentration, $n = 14$; high azide concentration, $n = 11$. See also Supplemental Movie 2.
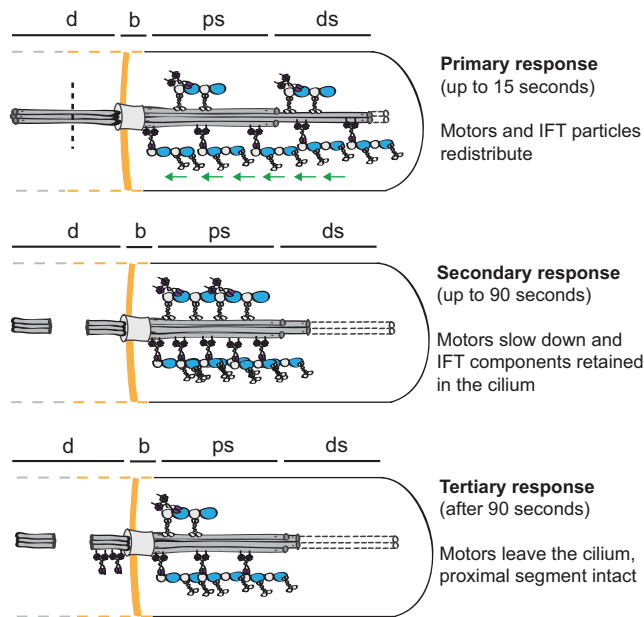
FIGURE 5: Multistep ciliary response to dendritic ablation. Cartoon schematic showing the three steps of the ciliary response to dendritic ablation: primary (motor redistribution), secondary (slowdown of IFT, effect of ATP depletion), and tertiary response (motor efflux, effect of ATP depletion); d, sensory dendrite; b, base; ps, proximal segment; ds, distal segment.

a *Chlamydomonas* kinesin-II subunit, is calcium dependent (Liang et al., 2014). As such, calcium signaling is proposed to play a key role in modulating IFT entry, assembly rate, and length (Liang et al., 2014, 2018). Further experiments in *Chlamydomonas* using a labeled calcium indicator have shown that a compartmentalized increase in Ca^{2+} can trigger retrograde IFT (Collingridge et al., 2013). Collectively, these and other studies provide mounting evidence that calcium signaling plays an important role in the regulation of IFT and ciliary functioning. It is possible that laser ablation acts as a cue to activate a calcium signaling pathway directly, or indirectly through the leaking of extracellular Ca^{2+} through the ablation site. In our experiments, however, we find that the rapid redistribution of IFT components following femtosecond-laser ablation is not affected by depleting Ca^{2+} outside the worm using EGTA. Although EGTA-based Ca^{2+} depletion in *C. elegans* has been previously described at similar concentrations and under a procedure similar to that used here (O'Halloran et al., 2009; Crook et al., 2013), more precise tools might be required to probe the pathways underlying the ciliary response to perturbation. Examples include genetically encoded Ca^{2+} indicators (Tian et al., 2009; Chalasani et al., 2010; Inoue et al., 2015; Hara-Kuge et al., 2018) or other biosensors for second messengers such as cAMP and cGMP.

In conclusion, we have shown that dendritic ablation triggers a rapid molecular response in *C. elegans* chemosensory cilia, resulting in IFT-protein redistribution toward the ciliary base, reduced motor velocity, and distal segment retraction. By visualizing and quantifying the real-time ciliary response to perturbation at the molecular level, we provide new insights into ciliary trafficking and function.

MATERIALS AND METHODS
C. elegans maintenance and strains
C. elegans maintenance and genetic crosses were done using standard procedures. All strains were constructed using Mos1 mediated single copy insertion (MosSCI) as described previously (Frokjaer-Jensen et al., 2008; Prevo et al., 2015; Mijalkovic et al., 2017): EJP76 (vuaSi15 [pBP36; Posm-6::osm-6::EGFP; cb-unc-119(+)] I; unc-119(ed3) III; osm-6(p811) V); EJP212 (vuaSi26 [pJM6; Pxbx-1::xbx-1::EGFP; cb-unc-119(+)] I; vuaSi2 [pBP22; Posm-3::osm-3::mCherry; cb-unc-119(+)] II; osm-3(p802) IV; xbx-1(ok279) V); and EJP401 (vuaSi [pSA401; Ptbb-4::tbb-4::EGFP; cb-unc-119(+)] I; unc-119(ed3) III). Integration was confirmed by PCR on the regions spanning the insertion.

Femtosecond-laser ablation experiments
The instrument used was built around a Nikon Eclipse Ti-E inverted microscope, equipped with a computer-controlled sample stage, perfect focus and a Nikon Plan Apo IR, NA 1.27, 60× water immersion objective. For ablation, we used a mode-locked, Ti:sapphire laser system (Coherent, Mira 900 Femto/Verdi 10W) with wavelength tuned to 860–870 nm with pulse durations of approximately 150 fs. The beam was expanded using telescopes to fill the back aperture of the microscope objective and positioned using a piezoelectric tip/tilt scanning mirror (Physik Instrumente S-334). Epifluorescence microscopy measurements were performed using the same objective, using a 488- or 561-nm laser (Coherent Compass) for excitation and a sCMOS camera (Hamamatsu Orca Flash 4.0 V2) for detection.

For the femtosecond-laser ablation experiments in combination with Ca^{2+} chelation, an updated version of the instrument was used, with a different ablation laser system (Spectra-Physics Mai Tai HP, with a pulse width <100 fs and wavelength tuned to 800 nm), different fluorescence excitation lasers (488-nm laser diode and 561-nm DPSS laser, Oxxius), and a different sCMOS camera (Photometrics Prime BSI). Epifluorescence microscopy measurements and ablation were performed using a Nikon Plan Apo λ, NA 1.40, 60× oil objective.

We performed femtosecond-laser ablation on phasmid dendrites in the tails of *C. elegans* young adult hermaphrodites. The worms were anesthetized in 5 mM levamisole in M9 and immobilized on a 2% agarose in M9 pad covered with a 22 × 22 mm cover glass and sealed with VaLaP. The focus of the femtosecond laser was positioned 1–3 μm from the ciliary base in all worms. Each strain was imaged continuously from at least 5 s preablation to 60 or 90 s postablation. The worms that were not treated with EGTA (see below) were also imaged at 180, 300, and 600 s postablation (200 frames; 152 ms per frame).

Calcium chelation experiments
C. elegans young adult hermaphrodites were anesthetized in 5 mM levamisole in M9. After 10 min, the worms were washed three times with 100 mM EGTA in M9, incubated for another 10 min in the EGTA solution, and immediately followed by femtosecond-laser ablation as described above.

Azide treatment experiments
C. elegans young adult hermaphrodites were anesthetized in 5 mM levamisole in M9 and immobilized on a 2% agarose in M9 pad, which was positioned on a microscope slide with a central opening (AMIL Technologies). Sodium azide (5 μl) or control dosing solution (M9) was pipetted through the central opening. After dosing, the opening was covered with a 22 × 22 mm cover glass to prevent pad desiccation. Dosing solutions were prepared using sodium azide (Sigma-Aldrich; S2002) dissolved in M9 at high (1 M), medium (500 mM), and low (100 mM) concentrations. Throughout the article, qualitative concentration descriptions are used because dosing

azide concentrations are not equal to absolute azide concentrations inside the worms. As an estimate, the internal concentration of sodium azide inside worms and their cilia is likely at least one order of magnitude lower than the dosing concentration (Davies *et al.*, 2003). Fluorescence imaging was done using a custom-built epi-illuminated fluorescence microscope described previously in detail (Prevo *et al.*, 2015). Worms were imaged continuously from 15 s predosing to 60 s postdosing (152 ms per frame, 300 EM gain), and then at 180 and 600 s postdosing (for 150–200 frames; 152 ms per frame; 300 EM gain). For XBX-1::EGFP and OSM-3::mCherry, dual-color imaging was performed on strain EJP212 using the conditions above.

Image analysis

Images were analyzed using open source tools KymographDirect and KymographClear (Mangeol *et al.*, 2016). Fluorescence intensities were corrected for background and bleaching (all strains), as well as bleed through of EGFP fluorescence into the mCherry channel (EJP 212 strain in the azide treatment experiments) as described previously (Mijalkovic *et al.*, 2017). To quantify the relative number of IFT components in the cilium pre- and postablation or dosing, we determined the background-corrected integrated fluorescence intensity from image sequences using ImageJ and MATLAB (R2014a).

REFERENCES

Bae YK, Barr MM (2008). Sensory roles of neuronal cilia: cilia development, morphogenesis, and function in *C. elegans*. Front Biosci 13, 5959–5974.

Besschetnova TY, Kolpakova-Hart E, Guan Y, Zhou J, Olsen BR, Shah JV (2010). Identification of signaling pathways regulating primary cilium length and flow-mediated adaptation. Curr Biol 20, 182–187.

Bourgeois F, Ben-Yakar A (2008). Femtosecond laser nanoaxotomy properties and their effect on axonal recovery in *C. elegans*. Opt Express 16, 5963.

Buisson J, Chenouard N, Lagache T, Blisnick T, Olivo-Marin JC, Bastin P (2013). Intraflagellar transport proteins cycle between the flagellum and its base. J Cell Sci 126, 327–338.

Burghoorn J, Dekkers MP, Rademakers S, de Jong T, Willemsen R, Swoboda P, Jansen G (2010). Dauer pheromone and G-protein signaling modulate the coordination of intraflagellar transport kinesin motor proteins in *C. elegans*. J Cell Sci 123, 2077–2084.

Chalasani SH, Kato S, Albrecht DR, Nakagawa T, Abbott LF, Bargmann CI (2010). Neuropeptide feedback modifies odor-evoked dynamics in *Caenorhabditis elegans* olfactory neurons. Nat Neurosci 13, 615–621.

Chung SH, Clark DA, Gabel CV, Mazur E, Samuel AD (2006). The role of the AFD neuron in *C. elegans* thermotaxis analyzed using femtosecond laser ablation. BMC Neurosci 7, 30.

Chung SH, Schmalz A, Ruiz RC, Gabel CV, Mazur E (2013). Femtosecond laser ablation reveals antagonistic sensory and neuroendocrine signaling that underlie *C. elegans* behavior and development. Cell Rep 4, 316–326.

Clement CA, Ajbro KD, Koefoed K, Vestergaard ML, Veland IR, Henriques de Jesus MP, Pedersen LB, Benmerah A, Andersen CY, Larsen LA, *et al.* (2013). TGF-β signaling is associated with endocytosis at the pocket region of the primary cilium. Cell Rep 3, 1806–1814.

Collingridge P, Brownlee C, Wheeler GL (2013). Compartmentalized calcium signaling in cilia regulates intraflagellar transport. Curr Biol 23, 2311–2318.

Crook M, Upadhyay A, Hanna-Rose W (2013). Necrosis in *C. elegans*. Methods Mol Biol 1004, 171–182.

Dalfo D, Michaelson D, Hubbard EJ (2012). Sensory regulation of the *C. elegans* germline through TGF-β-dependent signaling in the niche. Curr Biol 22, 712–719.

Davies AG, Pierce-Shimomura JT, Kim H, VanHoven MK, Thiele TR, Bonci A, Bargmann CI, McIntire SL (2003). A central role of the BK potassium channel in behavioral responses to ethanol in *C. elegans*. Cell 115, 655–666.

Frokjaer-Jensen C, Davis MW, Hopkins CE, Newman BJ, Thummel JM, Olesen SP, Grunnet M, Jorgensen EM (2008). Single-copy insertion of transgenes in *Caenorhabditis elegans*. Nat Genet 40, 1375–1383.

Gattass RR, Mazur E (2008). Femtosecond laser micromachining in transparent materials. Nat Photon 2, 219–225.

Gilbert SP, Webb MR, Brune M, Johnson KA (1995). Pathway of processive ATP hydrolysis by kinesin. Nature 373, 671–676.

Hao L, Thein M, Brust-Mascher I, Civelekoglu-Scholey G, Lu Y, Acar S, Prevo B, Shaham S, Scholey JM (2011). Intraflagellar transport delivers tubulin isotypes to sensory cilium middle and distal segments. Nat Cell Biol 13, 790–798.

Hara-Kuge S, Nishihara T, Matsuda T, Kitazono T, Teramoto T, Nagai T, Ishihara T (2018). An improved inverse-type Ca²⁺ indicator can detect putative neuronal inhibition in *Caenorhabditis elegans* by increasing signal intensity upon Ca²⁺ decrease. PLoS One 13, e0194707.

Hsu SC, Molday RS (1991). Glycolytic enzymes and a GLUT-1 glucose transporter in the outer segments of rod and cone photoreceptor cells. J Biol Chem 266, 21745–21752.

Imanishi M, Endres NF, Gennerich A, Vale RD (2006). Autoinhibition regulates the motility of the *C. elegans* intraflagellar transport motor OSM-3. J Cell Biol 174, 931–937.

Inoue M, Takeuchi A, Horigane S, Ohkura M, Gengyo-Ando K, Fujii H, Kamijo S, Takemoto-Kimura S, Kano M, Nakai J, *et al.* (2015). Rational design of a high-affinity, fast, red calcium indicator R-CaMP2. Nat Methods 12, 64–70.

Johnson KA (1983). The pathway of ATP hydrolysis by dynein. Kinetics of a presteady state phosphate burst. J Biol Chem 258, 13825–13832.

Johnson KA, Rosenbaum JL (1993). Flagellar regeneration in *Chlamydomonas*: a model system for studying organelle assembly. Trends Cell Biol 3, 156–161.

Liang Y, Pang Y, Wu Q, Hu Z, Han X, Xu Y, Deng H, Pan J (2014). FLA8/KIF3B phosphorylation regulates kinesin-II interaction with IFT-B to control IFT entry and turnaround. Dev Cell 30, 585–597.

Liang Y, Zhu X, Wu Q, Pan J (2018). Ciliary length sensing regulates IFT entry via changes in FLA8/KIF3B phosphorylation to control ciliary assembly. Curr Biol 28, 2429–2435.e2423.

Ludington WB, Ishikawa H, Serebrenik YV, Ritter A, Hernandez-Lopez RA, Gunzenhauser J, Kannegaard E, Marshall WF (2015). A systematic comparison of mathematical models for inherent measurement of ciliary length: how a cell can measure length and volume. Biophys J 108, 1361–1379.

Mangeol P, Prevo B, Peterman EJ (2016). KymographClear and Kymograph-Direct: two tools for the automated quantitative analysis of molecular and cellular dynamics using kymographs. Mol Biol Cell 27, 1948–1957.

Marshall WF, Rosenbaum JL (2001). Intraflagellar transport balances continuous turnover of outer doublet microtubules: implications for flagellar length control. J Cell Biol 155, 405–414.

Mijalkovic J (2018). Ensemble and Single-Molecule Dynamics of Intraflagellar Transport in *C. elegans*. PhD Thesis. Amsterdam: Physics and Astronomy, Vrije Universiteit Amsterdam.

Mijalkovic J, Prevo B, Oswald F, Mangeol P, Peterman EJ (2017). Ensemble and single-molecule dynamics of IFT dynein in *Caenorhabditis elegans* cilia. Nat Commun 8, 14591.

Mitchell BF, Pedersen LB, Feely M, Rosenbaum JL, Mitchell DR (2005). ATP production in *Chlamydomonas reinhardtii* flagella by glycolytic enzymes. Mol Biol Cell 16, 4509–4518.

Mukhopadhyay S, Lu Y, Shaham S, Sengupta P (2008). Sensory signaling-dependent remodeling of olfactory cilia architecture in *C. elegans*. Dev Cell 14, 762–774.

Nachury MV, Mick DU (2019). Establishing and regulating the composition of cilia for signal transduction. Nat Rev Mol Cell Biol 20, 389–405.

Nachury MV, Seeley ES, Jin H (2010). Trafficking to the ciliary membrane: how to get across the periciliary diffusion barrier? Annu Rev Cell Dev Biol 26, 59–87.

O'Halloran DM, Altshuler-Keylin S, Lee JI, L'Etoile ND (2009). Regulators of AWC-mediated olfactory plasticity in *Caenorhabditis elegans*. PLoS Genet 5, e1000761.

Pan X, Ou G, Civelekoglu-Scholey G, Blacque OE, Endres NF, Tao L, Mogilner A, Leroux MR, Vale RD, Scholey JM (2006). Mechanism of transport of IFT particles in *C. elegans* cilia by the concerted action of kinesin-II and OSM-3 motors. J Cell Biol 174, 1035–1045.

Pazour GJ, Witman GB (2003). The vertebrate primary cilium is a sensory organelle. Curr Opin Cell Biol 15, 105–110.

Perkins LA, Hedgecock EM, Thomson JN, Culotti JG (1986). Mutant sensory cilia in the nematode *Caenorhabditis elegans*. Dev Biol 117, 456–487.

Prevo B, Mangeol P, Oswald F, Scholey JM, Peterman EJ (2015). Functional differentiation of cooperating kinesin-2 motors orchestrates cargo import and transport in *C. elegans* cilia. Nat Cell Biol 17, 1536–1545.

Qin H, Burnette DT, Bae YK, Forscher P, Barr MM, Rosenbaum JL (2005). Intraflagellar transport is required for the vectorial movement of TRPV channels in the ciliary membrane. Curr Biol 15, 1695–1699.

Qin H, Diener DR, Geimer S, Cole DG, Rosenbaum JL (2004). Intraflagellar transport (IFT) cargo: IFT transports flagellar precursors to the tip and turnover products to the cell body. J Cell Biol 164, 255–266.

Schafer JC, Haycraft CJ, Thomas JH, Yoder BK, Swoboda P (2003). XBX-1 encodes a dynein light intermediate chain required for retrograde intraflagellar transport and cilia assembly in *Caenorhabditis elegans*. Mol Biol Cell 14, 2057–2070.

Schneider L, Clement CA, Teilmann SC, Pazour GJ, Hoffmann EK, Satir P, Christensen ST (2005). PDGFRαα signaling is regulated through the primary cilium in fibroblasts. Curr Biol 15, 1861–1866.

Scholey JM (2003). Intraflagellar transport. Annu Rev Cell Dev Biol 19, 423–443.

Schou KB, Pedersen LB, Christensen ST (2015). Ins and outs of GPCR signaling in primary cilia. EMBO Rep 16, 1099–1113.

Signor D, Wedaman KP, Orozco JT, Dwyer ND, Bargmann CI, Rose LS, Scholey JM (1999). Role of a class DHC1b dynein in retrograde transport of IFT motors and IFT raft particles along cilia, but not dendrites, in chemosensory neurons of living *Caenorhabditis elegans*. J Cell Biol 147, 519–530.

Singla V, Reiter JF (2006). The primary cilium as the cell's antenna: signaling at a sensory organelle. Science 313, 629–633.

Snow JJ, Ou G, Gunnarson AL, Walker MR, Zhou HM, Brust-Mascher I, Scholey JM (2004). Two anterograde intraflagellar transport motors cooperate to build sensory cilia on *C. elegans* neurons. Nat Cell Biol 6, 1109–1113.

Solter KM, Gibor A (1978). The relationship between tonicity and flagellar length. Nature 275, 651–652.

Tian L, Hires SA, Mao T, Huber D, Chiappe ME, Chalasani SH, Petreanu L, Akerboom J, McKinney SA, Schreiter ER, *et al.* (2009). Imaging neural activity in worms, flies and mice with improved GCaMP calcium indicators. Nat Methods 6, 875–881.

Vogel A, Noack J, Hüttman G, Paltauf G (2005). Mechanisms of femtosecond laser nanosurgery of cells and tissues. Appl Phys B 81, 1015–1047.

Wood CR, Rosenbaum JL (2014). Proteins of the ciliary axoneme are found on cytoplasmic membrane vesicles during growth of cilia. Curr Biol 24, 1114–1120.

Yanik MF, Cinar H, Cinar HN, Chisholm AD, Jin Y, Ben-Yakar A (2004). Neurosurgery: functional regeneration after laser axotomy. Nature 432, 822.

Ye F, Breslow DK, Koslover EF, Spakowitz AJ, Nelson WJ, Nachury MV (2013). Single molecule imaging reveals a major role for diffusion in the exploration of ciliary space by signaling receptors. eLife 2, e00654.